ISBN: 978-3-95450-201-1 doi:10.18429/JACoW-IBIC2018-WEPB18

PERFORMANCE OF A REFLECTIVE MICROSCOPE OBJECTIVE IN AN X-RAY PINHOLE CAMERA

L. Bobb *, G. Rehm, Diamond Light Source, Oxfordshire, U.K.

Abstract

X-ray pinhole cameras are used to measure the transverse beam profile of the electron beam in the storage ring from which the emittance is calculated. As improvements to the accelerator lattice reduce the beam emittance, e.g. with upgrades to fourth generation synchrotron light sources, likewise the beam size will be reduced such that micron and sub-micron scale resolution is required for beam size measurement. Therefore the spatial resolution of the pinhole camera imaging system must be improved accordingly. Here, the performance of a reflective microscope objective is compared to the high quality refractive lens which is currently in use to image the scintillator screen to the camera. The modulation transfer functions for each system have been assessed and will be discussed.

INTRODUCTION

There are three pinhole cameras in operation at Diamond Light Source: two of these systems continuously monitor the beam size [1] for vertical emittance feedback [2], whilst the third pinhole camera is installed on the Diagnostics X-ray beamline for research and development.

All of the pinhole cameras share a common layout in the storage ring as shown in Fig. 1. For each pinhole camera, synchrotron radiation from a bending magnet passes from vacuum to air through a 1 mm thick aluminium window. The spectrum has a photon energy range from 15 keV to approximately 60 keV and a peak at 25 keV. The X-rays then pass through the ≈24 µm pinhole aperture which is formed using a stacked arrangement of tungsten blades separated by chemically etched shims [3, 4]. The pinhole assembly is kept under nitrogen to prevent oxidation.

The first image plane is located at the scintillator screen which converts X-rays to visible photons. This image is relayed from the scintillator screen to the camera via a lens. The total path length is approximately 15 m.

The source-to-screen magnification is approximately 2.5. The horizontal beam size of the electron beam σ_x is ≈50 µm, therefore the horizontal beam size imaged at the scintillator screen is ≈125 µm. The electron beam profile which is approximated by a Gaussian extends much further than $\pm 1\sigma_x$, thus the field of view of the relay lens should be roughly an order of magnitude greater that the imaged beam size, in this case preferably 1 mm.

Rather than direct X-ray detection using an expensive detector, scintillator screens are incorporated to convert X-rays to visible photons which can be detected using machine vision CCD or CMOS cameras. In order to have a reasonable exposure time (< 100 ms), a sufficient intensity per pixel

* lorraine.bobb@diamond.ac.uk

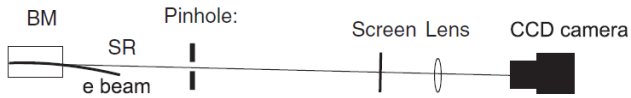

Figure 1: Schematic of the pinhole camera system [1]. A folding mirror is also typically included downstream of the scintillator such that the refractive lens and camera may be located away from the X-ray beam.

(i.e. light yield) to form an image above noise is required. This dictates the lower bound on the scintillator thickness for a given optical setup. The upper bound is determined by the spatial resolution that is required for imaging the electron beam. In some cases direct X-ray detection is necessary [5].

For pinhole cameras at third generation synchrotron light sources, the scintillator thickness is in the 100 to 500 µm range [1, 6]. Due to the limited information provided in the technical specifications from manufacturers, a series of experiments to compare and characterise different scintillator materials have been conducted largely by G. Kube *et al.* [7, 8]. These results have shown that although there is some variation of the spatial resolution for different materials, reducing the thickness of the scintillator provides the greatest improvement in spatial resolution [9].

The Point Spread Function (PSF) describes the spatial resolution of an imaging system. For pinhole cameras each optical element contributes to the overall PSF of the imaging system [3]. Using a Gaussian approximation the overall PSF may be represented as

$$\sigma^2_{\mathrm{PSF}} = \sigma^2_{\mathrm{pinhole}} + \sigma^2_{\mathrm{camera}} \tag{1}$$

with

$$\sigma^2_{\mathrm{pinhole}} = \sigma^2_{\mathrm{diffraction}} + \sigma^2_{\mathrm{aperture}} \tag{2}$$

and

$$\sigma^2_{\mathrm{camera}} = \sigma^2_{\mathrm{screen}} + \sigma^2_{\mathrm{lens}} + \sigma^2_{\mathrm{sensor}} \tag{3}$$

where the subscripts denote the sources of the PSF contributions [4]. The PSF contribution associated with imaging the scintillator screen denoted σ_{camera} may be measured using a knife-edge and uniform illumination. The PSF contribution from the pinhole denoted $\sigma_{\mathrm{pinhole}}$ may be calculated provided the aperture size is known [1].

The overall PSF is dominated by the contribution due to pinhole aperture size $\sigma_{\mathrm{pinhole}}$ and the contribution from the scintillator screen σ_{screen}. Investigations are under way to minimise $\sigma_{\mathrm{pinhole}}$ by improving the control of the pinhole aperture size using alternative fabrication methods such that the optimal size is used given the X-ray spectrum [4, 10].

ISBN: 978-3-95450-201-1 doi:10.18429/JACoW-IBIC2018-WEPB18

In this paper we focus on minimising σ_{screen} which is primarily dependent upon the scintillator thickness. Reducing the scintillator thickness causes a reduction in the light yield. Therefore we propose to replace the refractive lens with a microscope objective which has a significantly larger numerical aperture (NA). Given that the working distance of microscope objectives is small (< 40 mm), the optic must be placed in the path of the X-ray beam. For this reason, a refractive microscope objective is avoided since radiation damage will cause browning of the glass over time. Instead a reflective microscope objective is implemented. In the following sections, the spatial resolution of the reflective microscope objective imager is compared to the refractive lens imager.

EXPERIMENTAL SETUP

In the Lab

A schematic overview for each imager as tested in the lab is shown in Figs. 2 and 3. The test target is a negative USAF 1951 target which was backlit with a diffused white light source. Using the test target, the magnification and modulation transfer function (MTF) of each imager were measured.

In the refractive lens setup, a Schneider-Kreuznach Componon-S 2.8/50 lens is used to image the object plane (test target) to a FireWire Point Grey FLEA2 camera. This camera has an ICX204 CCD sensor with an absolute sensitivity threshold of 30 photons. The absolute sensitivity threshold may be approximated as the ratio between the dark noise and the quantum efficiency. This lens is well suited for 1:1 macro imaging. The technical specification of the refractive lens is summarised in Table 1.

From the MTF reported by the manufacturer, the refractive lens has the best spatial resolution when the iris aperture is at a minimum such that the f-number $f/\# = 8$ [11]. Given that

$$f/\# \approx \frac{1}{2NA} \tag{4}$$

the NA of the refractive lens is 0.06.

The technical specification of the reflective microscope objective is given in Table 1. The objective is coupled to a GigE Manta G319B camera which has an IMX265 CMOS sensor and absolute sensitivity threshold of 5 photons.

In the Tunnel

For testing with the X-ray pinhole camera and measurement of the PSF, both the refractive and reflective imagers were installed side by side on a translation stage in the tunnel such that they could be remotely inserted into the X-ray beam path. This ensures that the PSF contribution from the pinhole σ_{pinhole} is constant.

A 25 µm LuAg:Ce scintillator screen was installed on the reflective microscope objective imager and a 200 µm LuAg:Ce screen was installed on the refractive imager. Using XOP [13] to calculate the normalised power absorbed

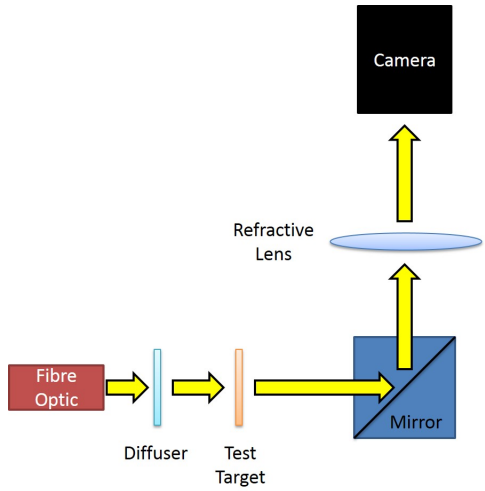

Figure 2: Schematic of the refractive imager.

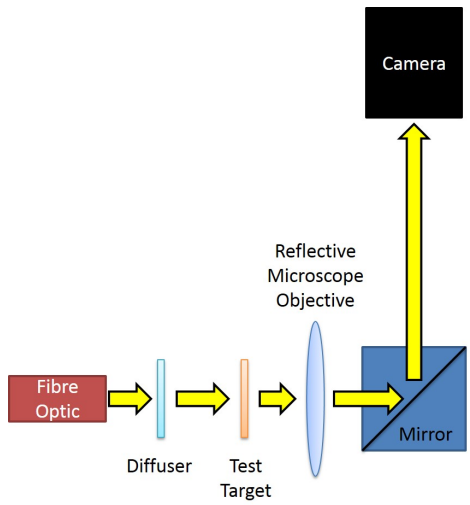

Figure 3: Schematic of the reflective microscope objective imager.

as a function of scintillator thickness, it is estimated that the light yield from the 25 µm is a factor of 3 less than that from the 200 µm LuAg:Ce screen.

The numerical aperture of the reflective microscope objective is a factor of 6.7 larger than the refractive lens. The absolute sensitivity threshold of the Manta G319B camera in the reflective objective imager is 6 times more sensitive to incident photons in comparison to the FLEA2 camera in the refractive imager.

MODULATION TRANSFER FUNCTION

The MTF (or spatial frequency response) is the magnitude response of the optical system to sinusoids of different spatial frequencies [14]. Using the back illuminated setups shown in Figs. 2 and 3, images of a negative USAF 1951 target were acquired. A diffuser is used to ensure uniform illumination of the target. The test target is rotated relative to the pixels of the camera sensor such that the MTF may be obtained using the

ISBN: 978-3-95450-201-1 doi:10.18429/JACoW-IBIC2018-WEPB18

Table 1: Technical specifications of the Schneider Componon-S 2.8/50 refractive lens and Newport 50105-01 reflective microscope objective [11, 12] where an asterisk indicates calculated values.

Parameter	Refractive lens	Reflective microscope objective
F-number	2.8 to 8	1.25*
Numerical Aperture	0.18 to 0.06*	0.4
Focal length	50.2 mm	160 mm (back) 13 mm (effective)
Working Distance	-	24 mm
Magnification	1	15
Transmission	400 - 700 nm	200 - 1000 nm

slanted-edge method [15]. The QuickMTF program [16] was used for the image analysis. The results were then exported to MATLAB.

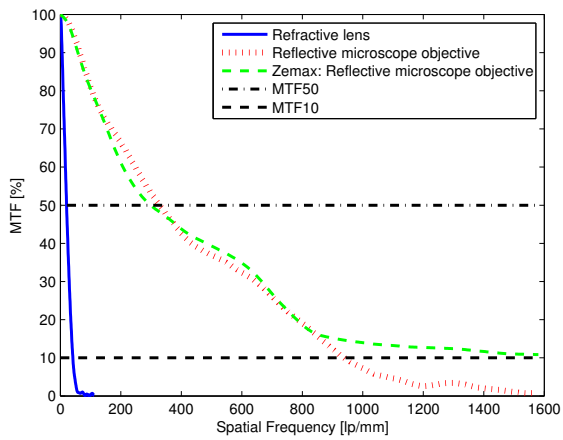

Figure 4: Comparison of the measured MTF of the refractive lens and the reflective microscope objective. Also plotted is the expected MTF from Zemax for a similar microscope objective from Thorlabs.

In order to compare the refractive lens and the reflective microscope objective the screen-to-camera magnification must be taken into account. Using the test target the magnifications of the refractive lens and reflective microscope objective were measured to be 1.04 and 14.7 respectively. Although not shown here, it was verified that the different camera sensors had a negligible impact on the measured MTF. The pixel size of the camera sensor determines the Nyquist frequency.

In Fig. 4 the MTFs of the imagers at the object plane (scintillator screen) are shown. As expected the microscope objective outperforms the refractive lens. If the resolution threshold is taken at MTF10, the maximum resolvable spatial frequencies for the refractive lens and reflective microscope objective are 42 lp/mm and 936 lp/mm respectively. In addition, the MTF from a similar microscope objective from Thorlabs for which a Zemax file was available is in good agreement with the measurement.

POINT SPREAD FUNCTION MEASUREMENT

Readers are referred to the "PSF measurement using the Touschek lifetime" section described in [4]. A summary of this method will be described here.

For a Touschek dominated beam (e.g. 400 bunches and 200 mA), the vertical beam size is approximately proportional to the beam lifetime τ (or condition). In this case the measured vertical beam size is

$$\sigma_M = \sqrt{(k\tau)^2 + \sigma_{PSF}^2} \tag{5}$$

where k is a scaling factor which relates to the lattice parameters at the source point.

After performing a LOCO on the storage ring to ensure the machine is in agreement with the accelerator model, the skew quads were adjusted using the VEFB controls to gradually change the vertical beam size. During this scan, for each beam size three images with corresponding beam conditions were recorded on pinhole camera 3. The first scan, denoted CAL 1, had the reflective microscope imager in the beam path. The second scan, denoted CAL 2, had the refractive imager in the beam path.

To obtain the measured vertical beam size from each image, the transverse profile was fitted with a 2D Gaussian and scaled using the measured source-to-screen and screen-to-camera magnifications. These magnifications were measured by remotely displacing the pinhole and imager respectively and observing the change in centroid position of the X-ray beam. The measured source-to-screen magnification was 2.47. The measured screen-to-camera magnifications were 1 (refractive imager) and 11 (reflective microscope imager). A least squares fit using Eq. 5 with k and σ_{PSF} as free parameters was then applied to each dataset

To monitor the stability of the machine and check the reproducibility of the calibration method, data was also acquired from pinhole cameras 1 and 2. Since no changes were made to these systems, the measured k and σ_{PSF} obtained from each calibration should not change between calibrations.

The calibration datasets from the three pinhole cameras are shown in Fig. 5. For each dataset, the results of the fit are reported in Table 2. Note that comparisons between the pinhole cameras should not be made. This is due to the

ISBN: 978-3-95450-201-1 doi:10.18429/JACoW-IBIC2018-WEPB18

Table 2: Results of the PSF measurement for each pinhole camera.

Pinhole camera	CAL 1		CAL 2	
	k [µm/mA/h]	σ_{PSF} [µm]	k [µm/mA/h]	σ_{PSF} [µm]
1	0.026	7.8	0.026	8.6
2	0.031	7.2	0.031	7.5
3	0.025	7.4	0.026	10.9
	Reflective microscope imager		**Refractive lens imager**	

differences in the optical elements of each pinhole camera, such that the PSF contributions shown in Eq. 1 are unique to each system. Furthermore, 200 µm Prelude420 (LYSO:Ce) scintillator screens, rather than LuAG:Ce, are installed on pinhole cameras 1 and 2. Remote focussing of the refractive lens is also available on pinholes 1 and 2, but is not present on pinhole 3. Thus comparisons should only be made between the two calibrations of each pinhole camera.

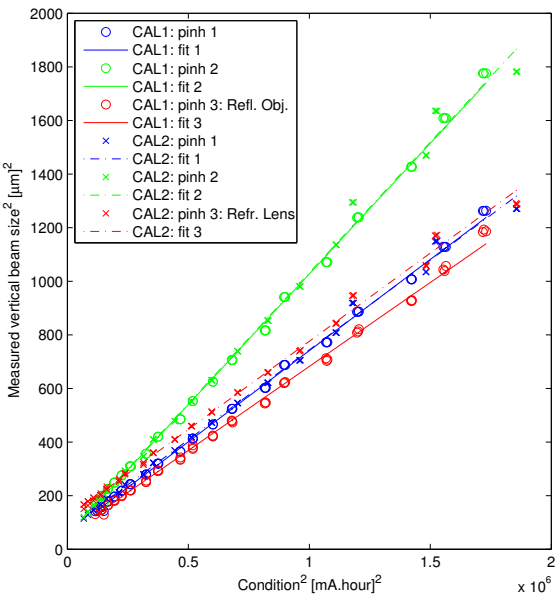

Figure 5: Results of the two calibrations for the three pinhole cameras. On pinhole camera 3, the reflective microscope imager and refractive lens imager were in operation for calibrations 1 and 2 respectively.

In Table 2 it is seen that the parameter k is reproducible to 0.001 precision for all three pinhole cameras. This indicates that the machine parameters were stable throughout the calibration period. Each calibration takes approximately 1 hour since it takes a few minutes for the reading of the beam lifetime to stabilise at each vertical beam size of the scan.

The PSF measurements from pinhole 3 show that an improvement of 30 % is achieved by replacing the 200 µm screen and refractive lens, with a 25 µm screen and reflective microscope objective. Averaging the difference of the PSF measurements for pinhole cameras 1 and 2 shows that the average error on σ_{PSF} is 0.5 µm.

Similar exposure times, typically tens of milliseconds, were used on the FLEA2 and Manta cameras to ensure each image contained roughly the same error from beam jitter. The gain was not changed during the calibration scans. At maximum camera gain the photon yield from the 25 µm screen was sufficient to operate the Manta camera in the reflective imager setup with an exposure time < 10 ms.

Further improvements to the spatial resolution could be achieved by using a thinner (< 25 µm) scintillator screen since the photon flux was more than sufficient given the large numerical aperture of the reflective imager. Additionally, it is known that the depth of field scales inversely with numerical aperture. Thus a scintillator with thickness ≤ 10 µm would be more suitable.

CONCLUSION

The spatial resolution of pinhole cameras must be improved for operation in future light sources. Although the fundamental limitation arises from the pinhole aperture itself, another important contribution to the overall point spread function comes from the scintillator screen. Depending upon budget and given a large source-to-screen magnification, direct imaging of the X-ray beam would inherently remove this point spread function contribution however, such detectors are significantly more expensive and tend to have a large pixel size. Instead, the results presented in this paper show that a thin scintillator screen coupled with a reflective microscope objective which has a large numerical aperture can provide a significant reduction to the overall PSF of the pinhole camera whilst maintaining the frame rates needed for online feedback.

REFERENCES

[1] C. Thomas et al., "X-ray pinhole camera resolution and emittance measurement", Phys. Rev. ST Accel. Beams 13, 022805, (2010).

[2] I.P.S. Martin et al., "Operating the Diamond Storage Ring with Reduced Vertical Emittance", Proc. of IPAC2013, Shanghai, China, MOPEA071.

[3] P. Elleaume et al., "Measuring Beam Sizes and Ultra-Small Electron Emittances Using an X-ray Pinhole Camera", J. Synchrotron Rad., (1995). 2, 209-214.

ISBN: 978-3-95450-201-1 doi:10.18429/JACoW-IBIC2018-WEPB18

[4] L.M. Bobb et al., "Performance Evaluation of Molybdenum Blades in an X-ray Pinhole Camera", Proc. of IBIC2016, Barcelona, Spain, WEPG63.

[5] B. Yang et al., "High Energy X-ray Pinhole Camera for High Resolution Electron Beam Size Measurements", Proc. of IBIC2016, Barcelona, Spain, TUPG66.

[6] F. Ewald et al., "Vertical Emittance Measurement at the ESRF", Proc. of DIPAC2011, Hamburg, Germany, MOPD61.

[7] G. Kube et al., "Inorganic Scintillators for Particle Beam Profile Diagnostics of Highly Brilliant and Highly Energetic Electron Beams", Proc. of IPAC2012, New Orleans, Louisiana, USA, WEOA02.

[8] G. Kube et al., "Resolution Studies of Inorganic Scintillation Screens for High Energy and High Brilliance Electron Beams", Proc. of IPAC2010, Kyoto, Japan, MOPD088.

[9] G. Kube, "High Resolution Scintillating Screens for Measurements of few Micrometer Beams", Topical Workshop on Emittance Measurements for Light Sources and FELs, ALBA, 2018.

[10] L.M. Bobb et al., "Beam Size Measurement Using High Aspect Ratio LIGA Apertures in an X-ray Pinhole Camera", Proc. of IPAC2017, Copenhagen, Denmark, MOPAB132.

[11] Schneider-Kreuznach, Componon-S 2.8/50, http://www.schneiderkreuznach.com/en/industrial-solutions/lenses-and-accessories/products/unifoc-system/v-mount-macro-lenses/componon-s-2850/

[12] Newport Reflective Microscope Objectives, https://www.newport.com/f/reflective-microscope-objectives

[13] XOP, http://www.esrf.eu/Instrumentation/software/data-analysis/xop2.4

[14] G.D. Boreman, "Modulation Transfer Function in Optical and Electro-Optical Systems", SPIE Press, Bellingham, WA (2001).

[15] E. Buhr et al., "Simple method for modulation transfer function determination of digital imaging detectors from edge images", Proc. SPIE 5030, Medical Imaging 2003: Physics of Medical Imaging, 877.

[16] QuickMTF, http://www.quickmtf.com/